

Chapter 5

Strong interactions of single atoms and photons near a dielectric boundary

This chapter is largely based on Ref. [5]. Reference [5] refers to the then current literature in 2011 at the time of publication. The work described in this chapter is a result of our team collaboration of seven authors of the manuscript, whose contributions I would like to acknowledge here. Hansuek Lee and Eric Ostby (Vahala group) contributed to the fabrication of microtoroidal resonator devices and sharing of expertise in optical coupling using the tapered fiber central to our experiment. Nate Stern and I contributed to carrying out the experiment, implementing critical modifications that build upon the setup discussed in chapter 4 and developed by Takao Aoki and myself, conducting measurements, data analysis, and developing strongly coupled atom near surface models. In our numerical work, Nate Stern contributed mainly to the calculation of Casimir-Polder phenomena, and I contributed mainly to the entire system simulation. This work was carried out under the guidance and supervision of my advisor, Prof. Jeff Kimble, in collaboration with Prof. Kerry Vahala at Caltech.

5.1 Introduction

Cavity quantum electrodynamics (cQED) provides the setting for quantum control of strong interactions between a single atom and one photon. Many such atom-cavity systems interacting through coherent exchanges of single photons could be the basis for scalable quantum networks. However, moving beyond current proof-of-principle experiments involving just one or two conventional optical cavities requires the localization of individual atoms at distances $\lesssim 100$ nm from a resonator's

surface. In this regime an atom can be strongly coupled to a single intracavity photon while at the same time experiencing significant radiative interactions with the dielectric boundaries of the resonator. Here, we present observations of strongly coupled single atom-photon dynamics in a cavity QED setting using real-time detection and high-bandwidth feedback to select and monitor single cesium atoms located ~ 100 nm from the surface of a micro-toroidal optical resonator. Strong radiative interactions of atom and cavity field probe atomic motion through the evanescent field of the resonator and reveal both the significant role of Casimir-Polder attraction and the manifestly quantum nature of the atom-cavity dynamics.

5.2 Background

The proximity of dielectric boundaries fundamentally alters atomic radiative processes as compared to quantum electrodynamics in free space. For example, free-space Lamb shifts and Einstein- A coefficients (i.e., level positions and decay rates) are modified for atom-surface distances comparable to the relevant transition wavelengths, as considered in the pioneering analyses of Casimir and Polder [38] and of Purcell [190] in the late 1940s. Seminal experiments in the 1970s investigated radiative decay for organic dye molecules near a metal mirror [70] and were followed in the 1980s by landmark observations of the inhibition of spontaneous emission for a trapped electron [84] and an atom in a waveguide [109]. The ensuing years have witnessed the development of cavity quantum electrodynamics (cQED) in this *perturbative* regime of boundary-modified linewidths and level shifts [101, 231, 24], with applications ranging from measurements of fundamental constants [177] to the development of novel semiconductor devices [166].

With increased interaction strength, a *non-perturbative* regime of cQED becomes possible and is characterized not by the dominance of irreversible decay but rather by the cyclic, reversible exchange of excitation between atom and photon [114]. The experimental quest for strong atom-photon coupling had its initial success in 1985 in the microwave regime with the realization of the micromaser [164], with strong non-perturbative coupling in the optical domain achieved some years later [236]. Now, however, strong coupling has made possible the coherent control of atomic radiative dynamics on a photon-by-photon basis [167, 101]. Strong coupling has also been demonstrated for a wide class of physical systems [240] beyond single atoms, including quantum dots coupled to micropillars and photonic bandgap cavities [124] and Cooper-pairs interacting with superconducting resonators [216]. This non-perturbative regime of cQED with strong light-matter interactions mediated by single photons has led to new scientific capabilities, ranging from a laser that operates with one-and-

the-same atom [162] to the deterministic generation of entangled photon pairs [250] to a two-qubit superconducting quantum processor [63].

To a large degree, investigations of perturbative and non-perturbative cQED phenomena have been made independently. For example, for one atom located near the center of a Fabry-Perot cavity with volume $(l)^3 \sim (10 \mu\text{m})^3$, the coherent coupling g to an optical resonance can be large compared to radiative decay characterized by the Einstein- A coefficient and cavity loss rate κ , namely $g \gg (\gamma_0, \kappa)$ where $\gamma_0 = A/2$, placing the system in the regime of strong, non-perturbative atom-photon coupling [167, 86]. Nevertheless, corrections to the atomic Lamb shift and Einstein- A coefficient arising from surface interactions with the cavity boundaries remain small (e.g., $\delta A/A \sim 10^{-5}$). However, many applications in quantum information science [132] could benefit from strong atom-photon interactions with micro- and nano-scopic optical resonators [11, 200, 147, 224, 50, 73] integrated on atom chip devices [81, 193]. Atomic localization on a sub-wavelength scale near a resonator's surface is then required, with aspects of both perturbative and non-perturbative cQED necessarily coming into play.

In this chapter we investigate such a regime for single cesium atoms radiatively coupled to a high- Q microtoroidal cavity [9, 11] and in close proximity to the resonator's dielectric surface. As illustrated in Fig. 5.1(a), cold cesium atoms are released from an optical dipole-force trap and randomly fall past the microtoroid. A real-time detection scheme based upon strong radiative interactions between one atom and the evanescent cavity field selects atomic trajectories passing within $d \lesssim 300$ nm from the resonator's surface, with a large fraction of atoms passing below 100 nm and crashing into the surface. On this scale, the atom's coherent interaction with the cavity field is characterized by strong, non-perturbative coupling [Fig. 5.1(b), 5.3 (c) (i)], which we demonstrate by direct measurements of so-called "vacuum-Rabi" spectra for light transmitted and reflected by the atom-cavity system, as well as by observations of photon antibunching for the transmitted light. On the other hand, the atom's motion and level structure are significantly influenced by the (perturbative) Casimir-Polder potential from the surface's proximity [Fig. 5.1 (c) (ii)], which we infer from measurements of the time dependence of the cavity transmission during an atomic transit event, as well as from modifications of the spectra recorded for the transmitted and reflected fields. These observations are in reasonable agreement with a theoretical model that we have implemented by Monte-Carlo simulation and which gives insight into the underlying atomic dynamics, as detailed in Sec. 5.10

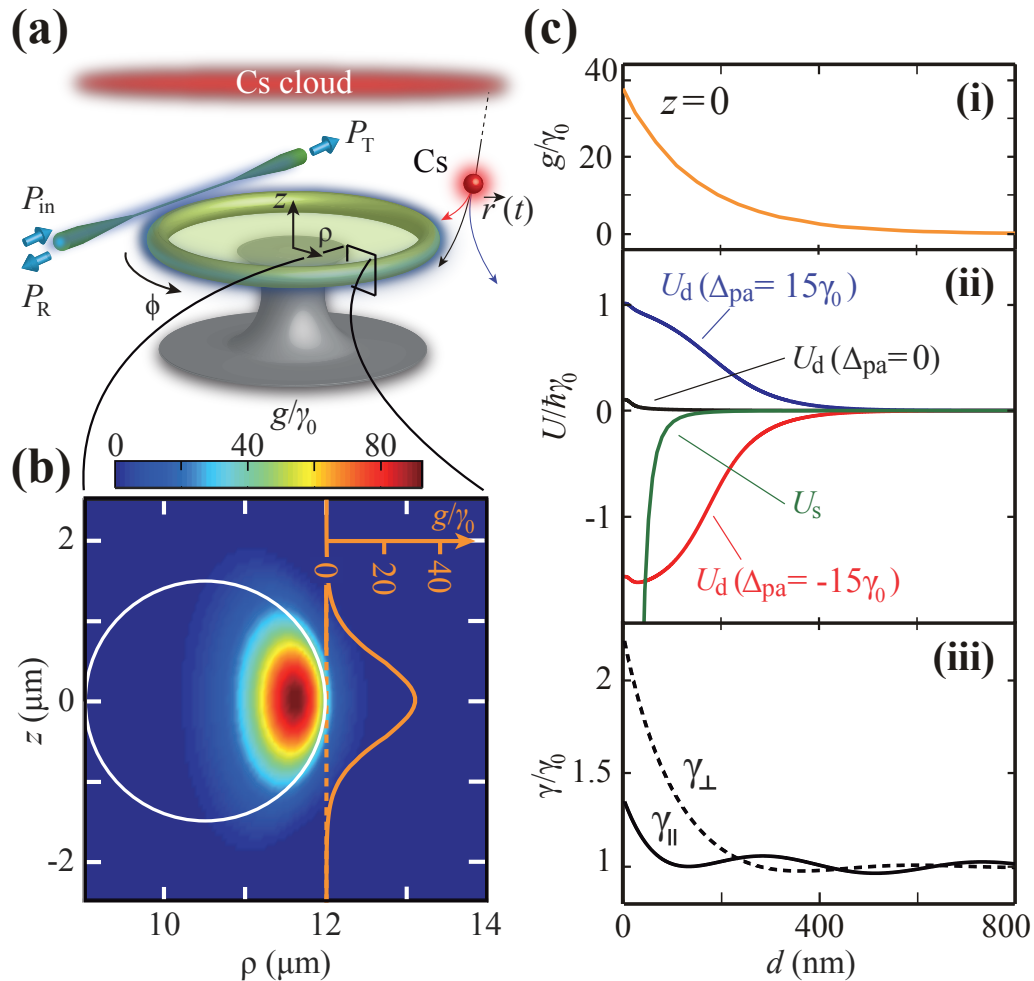


Figure 5.1: **Radiative interactions and optical potentials for an atom near the surface of a toroidal resonator.** (a) Simple overview of the experiment showing a cloud of cold cesium atoms released so that a few atoms fall within the evanescent field of a microtoroidal resonator. Light in a tapered optical fiber excites the resonator with input power P_{in} at frequency ω_p , leading to transmitted and reflected outputs $P_{\text{T}}, P_{\text{R}}$. (b) Cross section of the microtoroid at $\phi = 0$ showing the coherent coupling coefficient $|g(\vec{r}) = g(\rho, z, \phi)|$ for a TE polarized whispering-gallery mode. The microtoroid has principal and minor diameters $(D_p, D_m) = (24, 3) \mu\text{m}$, respectively. (c) (i) Coherent coupling $|g(d, z, \phi)|$ for the external evanescent field as a function of distance $d = \rho - D_p/2$ from the toroid's surface for $(z, \phi) = (0, 0)$. (ii) The effective dipole potentials U_d for resonant $\omega_p = \omega_a^{(0)}$, red $\omega_p < \omega_a^{(0)}$ and blue $\omega_p > \omega_a^{(0)}$ free-space detunings of the probe P_{in} (intracavity photon number ~ 0.1 , circulating power ~ 100 nW, circulating field intensity at surface $\sim 0.01 \mu\text{W}/\mu\text{m}^2$). The Casimir-Polder surface potential U_s for the ground state of atomic Cs is also shown. (iii) The atomic decay rate $\gamma(d)$ as a function of distance d from the toroid's surface for TE (γ_{\parallel}) and TM (γ_{\perp}) modes. All rates in this figure are scaled to the decay rate in free space for the amplitude of the Cs $6P_{3/2} \rightarrow 6S_{1/2}$ transition, $\gamma_0/2\pi = 2.6$ MHz. The approximate distance scale probed in our experiment is $0 < d < 300$ nm.

5.3 Real time single atom detection

For the identification of atoms near the surface of the microtoroid in the regime shown in Fig. 5.1(c), we rely on the strong interaction of atom and cavity field to modify the light transmitted by the cavity. Specifically, because the atom-cavity coupling coefficient $g(\vec{r}(t))$ depends upon the atomic trajectory $\vec{r}(t)$, we can select single atoms located within the cavity mode by demanding a minimum criterion for the change in cavity transmission due to the atomic trajectory. Our scheme for single-atom detection is similar to that used in previous work [9, 57, 10], but with significant modifications. Namely, by implementing fast digital logic, we achieve reliable real-time identification of atomic transit events in times as short as 250 ns from the photoelectric counts due to the transmitted power $P_T(t)$. Note that this identification would not be possible for an atom in free space without the emission rate enhancement and efficiency afforded by coupling to the cavity. Given the identification of a falling atom, the control logic switches the power P_{in} and frequency ω_p of the probe input within $\simeq 100$ ns and records subsequent photoelectric counts for the transmitted $P_T(t)$ and reflected $P_R(t)$ outputs from the cavity. These records of photoelectric counts form the basis for the analysis that follows, with further details presented in Sec. 5.9.1.

To address experimentally the question of the distance scale for the recorded atom transit events, we first examine the time dependence of the cavity transmission $T(t) = P_T(t)/P_{\text{in}}$ immediately following a trigger heralding the arrival of an atom into the cavity mode. Figure 5.2 (a) shows $T(t)$ for the case of resonant excitation, namely $\Delta_{\text{pa}} = \omega_p - \omega_a^{(0)} = 0$ and $\Delta_{\text{ca}} = \omega_c - \omega_a^{(0)} = 0$, where $\omega_a^{(0)}$ is the free-space atomic frequency for the $6S_{1/2}, F = 4 \rightarrow 6P_{3/2}, F = 5$ transition in atomic Cs, ω_p is the incident laser probe frequency, and ω_c is the resonant frequency of the relevant toroidal cavity mode. Two characteristic decay times are evident, with the background subtracted transmission $T_B(t) \equiv T(t) - B$ fitted well by the sum of an exponential ($\propto e^{-t/\delta t_I}$) and a Gaussian ($\propto e^{-(t/\delta t_{II})^2}$). Here, the background level $B \equiv T(t \gg \delta t_{I,II})$ is determined from the cavity transmission for times long compared to the duration of the transit event, with $B/T(\Delta_{\text{pa}} \gg \kappa) \lesssim 0.01$.

The time constants $\delta t_I, \delta t_{II}$ can be associated with distance scales d_I, d_{II} by way of the average velocity \bar{v} with which atoms arrive at the toroid's mode following release from the optical trap, namely $\bar{v} \sim 0.17$ m/s, leading to $d_I \simeq 130$ nm and $d_{II} \simeq 640$ nm. For comparison, the scale length for $g(d)$ in the radial direction is $\lambda = 1/k_0 = 136$ nm (Fig. 5.1 (c) (i)), while in the vertical direction, the variation of $g(z)$ is approximately Gaussian ($\propto e^{-(z/w_0)^2}$) with waist $w_0 \simeq 590$ nm (Fig. 5.1 (b)). The comparisons $d_I \sim \lambda$ and $d_{II} \sim w_0$ suggest that the short-lived component δt_I in Fig. 5.2 (a) arises from atomic trajectories that are deflected from their otherwise vertical fall to largely radial

paths of length λ that terminate at the dielectric surface. Similarly, the longer-lived component δt_{II} is associated with trajectories that pass along z without significant radial motion toward the surface of the toroid.

Of course an atom near the surface will not move with constant velocity but will be accelerated by interactions with surface potentials and the cavity field itself. To reach a quantitative understanding of the external, center-of-mass motion and the internal, atomic dipole-cavity field coupling, we have implemented a numerical simulation that incorporates both perturbative and non-perturbative aspects of the radiative interaction of the atom and micro-toroid. Our Monte-Carlo simulation draws random initial trajectories for atoms falling from a thermal cloud and implements a stochastic process for photoelectric detection to emulate our real-time detection technique. The model includes Casimir-Polder and dipole forces from the potentials $U_{\text{s}}(\vec{r}), U_{\text{d}}(\vec{r})$ shown in Fig. 5.1 (c) (ii), atomic level shifts (and hence detunings) from $U_{\text{s}}(\vec{r})$, and boundary-modified decay $\gamma_{\parallel}(d)$ shown in Fig. 5.1 (c) (iii). The non-perturbative interaction of atom and cavity field is based upon the analytic results in Ref. [9, 57]. Details of the simulation can be found in the Sec 5.10.2.

5.4 Experimental results

Results from this analysis are presented in Fig. 5.2 (b-e). In agreement with the observations in Fig. 5.2 (a), $T_B(t)$ from the simulation in Fig. 5.2 (b) exhibits two time scales and is fit well by the sum of an exponential and a Gaussian. Atomic trajectories associated with the $\delta t_{\text{I}}^{(s)}$ have distances peaking around $d_{\text{I}} \sim 100$ nm and terminate with crashes into the surface of the toroid [$p_{\text{I}}(d)$ in Fig. 5.2 (c)], but exhibit large coupling $g_{\text{I}}/2\pi \sim 40$ MHz [$p_{\text{I}}(g)$ in Fig. 5.2 (d)] and large surface-induced shifts of the atomic transition frequency $\delta_{\text{a,I}}/2\pi \gtrsim 10$ MHz for $d \lesssim 60$ nm [$p_{\text{I}}(\delta_{\text{a}})$ in Fig. 5.2 (e)]. By contrast, the complementary set of trajectories for $\delta t_{\text{II}}^{(s)}$ pass roughly vertically through the cavity mode along z (hence their Gaussian time dependence). Relative to the $\delta t_{\text{I}}^{(s)}$ set, these trajectories exhibit larger distances $d_{\text{II}} \sim 250$ nm, smaller coupling $g_{\text{II}}/2\pi \sim 20$ MHz, and surface-induced shifts of the atomic transition frequency $\delta_{\text{a,II}} \lesssim \gamma_0$ [$p_{\text{II}}(d), p_{\text{II}}(g), p_{\text{II}}(\delta_{\text{a}})$ in Figs. 5.2 (c-e), respectively].

In Fig. 5.3 we investigate temporal dynamics for the cavity transmission $T(t)$ but now with non-zero detuning between the atom and probe field, $\Delta_{\text{ca}}/2\pi = \Delta_{\text{pa}}/2\pi = \pm 40$ MHz (Fig. 5.3 (a)). Since $\omega_{\text{p}} \neq \omega_{\text{a}}$, dipole forces from coherent excitation of the intracavity field should induce an asymmetry for $T(t)$ for red and blue detuning, with faster decay for red detuning ($\omega_{\text{p}} < \omega_{\text{a}}$) due to the combined effect of the attractive potentials $U_{\text{s}}(\vec{r})$ and $U_{\text{d}}(\vec{r})$ shown in Fig. 5.1 (c) (ii). The

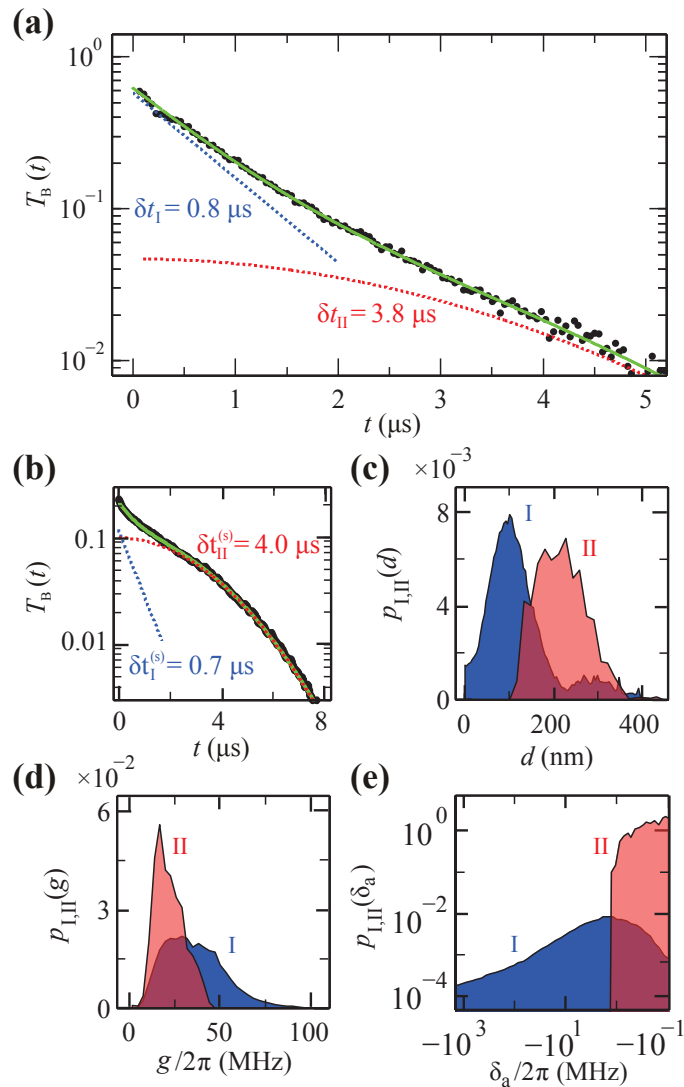


Figure 5.2: **Observation (a) and simulation (b-e) of atomic transits within the evanescent field of the micro-toroidal resonator for $\Delta_{ca} = \Delta_{pa} = 0$.** **a)** Observed cavity transmission $T_B(t)$ versus time t following a triggering event at $t = 0$, with approximately 5×10^4 triggered transits included. The data are fit to the sum of an exponential (I) and a Gaussian (II) (green curve), with time constants $\delta t_I = 0.78 \pm 0.02 \mu\text{s}$ and $\delta t_{II} = 3.75 \pm 0.09 \mu\text{s}$, with each component shown by the dotted lines. **(b)** Simulation result for 1000 triggered atoms for the cavity transmission $T_B^{(s)}(t)$ versus time t (points) from an ensemble of triggered trajectories. The green curve is a fit to the sum of an exponential and Gaussian with time constants $\delta t_I^{(s)} = 0.69 \mu\text{s}$, $\delta t_{II}^{(s)} = 4.0 \mu\text{s}$ while the dotted lines represent the individual fit components. **c-e)** Probability densities $p_i(d)$, $p_i(g)$, $p_i(\delta_a)$ for the distance d , coupling g , and transition frequency shift $\delta_a = \omega_a(d) - \omega_a^{(0)}$ from the same simulation set as for (b). $\{d, g, \delta_a\}$ are averaged over the first 500 ns following the trigger. For these results, the trajectories are divided into two classes based on simulated detection events for photon transmission, $i = \{I, II\}$ corresponding to the two time constants $\delta t_I^{(s)}$ (blue shaded curve) and $\delta t_{II}^{(s)}$ (red shaded curve) in (b). This is a stochastic division and hence the distributions and trajectory characteristics show some overlap between sets I and II. Note: Intracavity photon number ~ 0.1 , circulating power ~ 100 nW, circulating field intensity at surface $\sim 0.01 \mu\text{W}/\mu\text{m}^2$.

data are fit well by decaying exponentials ($\propto e^{-t/\delta t_i}$, $i = \{\text{red, blue}\}$). Also plotted are simulations of the experiment for freely falling atoms with $U_s = U_d = 0$, atoms under the influence of only dipole forces, $U_s = 0$, and a full simulation including both the dipole force and CP forces. For both red and blue detunings, the timescales from the simulation absent U_s, U_d are substantially longer than observed in experiment. In contrast with the case $\omega_p = \omega_a$ in Fig. 5.2, there is no significant Gaussian component of these temporal decays because of the difference in scale lengths of the CP potential U_s and effective dipole potential U_d ($\Delta_{ca} = \pm 15\gamma_0$), which become comparable to γ_0 for distances $d \lesssim \{65, 200\}$ nm, respectively (Fig. 5.1 (c) (ii)). Long range dipole forces, which are largely absent for Fig. 5.2, dominate the trajectory dynamics of Fig. 5.3 and consequently vertically falling long-lived Gaussian trajectories do not significantly contribute.

5.5 Atom trajectories near a microtoroid

To illustrate the underlying atomic motion, Fig. 5.3 (b) displays atomic trajectories projected onto the $\rho - z$ plane for the simulations in Fig. 5.3 (a), with each panel displaying a representative sample of untriggered and triggered trajectories. For red detuning, $\Delta_{pa} < 0$, introducing dipole forces and CP forces leads to every triggered atom crashing into the toroid surface, explaining the short decay δt_{red} . The blue detuned case is more complicated, with both attractive CP forces and the repulsive dipole force reducing the time the atom is in the mode; CP forces pull nearby atoms into the surface while the dipole force repels other atoms out of the mode.

As shown in Fig. 5.3 (c) and discussed in Sec. 5.9, we have augmented our numerical simulation to include a dipole force optical trap U_t (FORT) formed by the toroid's evanescent field [246, 201] in addition to the potentials U_s, U_d . The trapping potential U_t is triggered by the same criteria as for Figs. 5.3 (a), (b), with then a significant fraction of triggered atoms bound in orbit around the toroid for durations surpassing $50 \mu\text{s}$.

5.6 Spectral measurements

The measurements in Figs. 5.2, 5.3 rely upon strong interactions of atoms and photons for initial atomic localization within the cavity mode and for measurements of the subsequent motion by way of $T(t)$. To establish directly the non-perturbative coupling of atom and cavity field, we next turn to measurements of transmission $T(\omega_p) = P_T(\omega_p)/P_{\text{in}}$ and reflection $R(\omega_p) = P_R(\omega_p)/P_{\text{in}}$ spectra as functions of ω_p (Fig. 5.4). Probe spectra $\{T(\omega_p), R(\omega_p)\}$ are recorded following the detection of

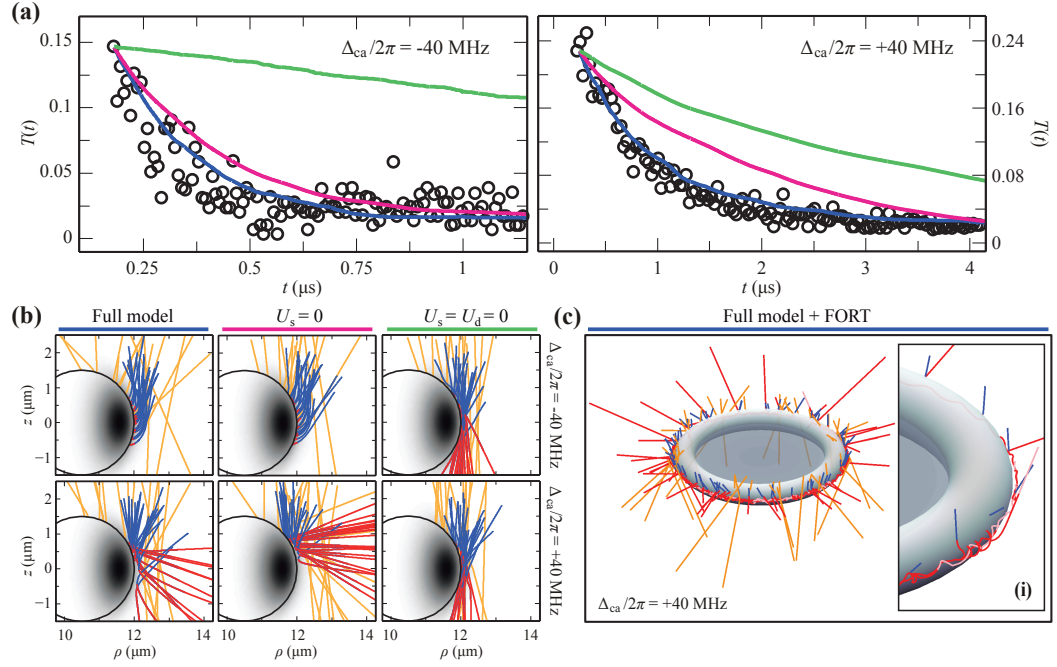


Figure 5.3: **Dynamics and trajectories for strongly coupled atoms moving in surface and dipole potentials $\{U_s, U_d\}$.** (a) Transmission $T(t)$ for $\Delta_{ca}/2\pi = -40$ MHz (left) and $+40$ MHz (right) measured after an atom trigger at $t = 0$. In each panel, the circles are data for 2×10^3 trigger events; the lines are simulations of $T(t)$ for the full model (blue), for $U_s = 0$ (magenta), and for $U_s = U_d = 0$ (green). Exponential fits to the data give time constants $\delta t_{\text{red}} = 0.11 \pm 0.01$ and $\delta t_{\text{blue}} = 0.53 \pm 0.03$ μs , while fits to the full simulation yield time constants $\delta t_{\text{red}}^{(s)} = 0.19 \pm 0.02$ μs and $\delta t_{\text{blue}}^{(s)} = 0.59 \pm 0.06$ μs , where quantitative differences are attributed to simplifications inherent in the simulation model (see SI). (b) Representative atomic trajectories projected onto the $\rho - z$ plane for simulations in panel (a), with the TE mode intensity plotted on a gray scale. The upper panels are for $\Delta_{ca}/2\pi = -40$ MHz while the lower panels are for $\Delta_{ca}/2\pi = +40$ MHz. The color bars at the top of the panels match the colors of the curves in (a). For each panel, orange lines are untriggered trajectories, while triggered trajectories are represented by blue lines which turn red after a trigger at $t = 0$. (c) Simulations showing trajectories from a full 3D simulation with U_s, U_d , as well as a two-color dipole potential (FORT) triggered “on” by atom detection at $t = 0$. $\Delta_{ca}/2\pi = +40$ MHz in correspondence to (a), (b). Blue lines represent falling atoms with the FORT beams “off” ($t < 0$), while red lines are trajectories after the FORT is triggered “on” and an atom begins to orbit the toroid. To illustrate the timescale, the trajectories are colored pink for $t > 50$ μs . Note: intracavity photon number ~ 0.1 , circulating power ~ 100 nW, circulating field intensity at surface ~ 0.01 $\mu\text{W}/\mu\text{m}^2$.

a single-atom event with $\omega_p = \omega_c$ for a fixed detuning Δ_{ca} between atom and cavity to optimize sensitivity for an intracavity atom (i.e., $\Delta_{ca} = \Delta_{pa}$). With an atom thereby present in the cavity mode, fast control logic and feedback switch the probe power P_{in} to some fiducial level for a given spectrum and the probe frequency ω_p to a relevant detuning $\Delta_{pa} \neq \Delta_{ca}$ for measurements of $\{T(\omega_p), R(\omega_p)\}$. The spectra are built up over thousands of transit detections and consequently represent an ensemble average over triggered atom trajectories.

Strong radiative coupling of an atom and a microtoroidal resonator is described by an extension of the Jaynes-Cummings [114, 9] Hamiltonian (see SI). Our whispering-gallery resonator supports two counter-propagating traveling-wave modes that are coupled by internal scattering at a rate h . The interaction of the cavity eigenmodes with an intracavity atom is characterized by coherent coupling $g(\vec{r})$, with the resulting atom-cavity eigenvalues $\{\lambda_i\}$ shown in Fig. 5.4 (a) for the single-excitation eigenstates. For large detuning $|\Delta_{ca}| \gg g$, there is one atom-like and two cavity-like eigenvalues. For $\Delta_{ca} \sim g$, there is an anti-crossing between the imaginary parts of two dressed-state eigenvalues λ_{\pm} with splitting $\Delta\lambda_{\pm} = \text{Im}(\lambda_+ - \lambda_-) \approx \sqrt{\Delta_{ca}^2 + 4g^2}$ for $g \gg \{h, \kappa, \gamma_{\parallel}\}$, while the third cavity-like eigenvalue λ_0 remains uncoupled to the atom. This dressed-state eigenstructure, along with the dissipative rates $\gamma_{\parallel}(d)$ and κ for atom and cavity, determine the system's spectral response $\{T(\omega_p), R(\omega_p)\}$.

Using a simple model with atoms falling vertically through the evanescent field of Fig. 5.1 (b) with $\{U_s, U_d\} = 0$ (SI), we construct a probability distribution $p_{\text{fall}}(g)$ of coupling constants for atom detection, with probe spectra $\{T(\omega_p), R(\omega_p)\}$ then obtained by averaging spectra for fixed g over the distribution $p_{\text{fall}}(g)$ (Fig. 5.4 (b)). Although the full eigenstructure from Fig. 5.4 (a) cannot be resolved due to the ‘smearing’ from $p_{\text{fall}}(g)$ even with $g_{\text{max}} \gg \{\kappa, \gamma_{\parallel}\}$, the splitting $\Delta\omega_{\text{peaks}}^{(b)}$ between λ_- and λ_0 (shifted by its proximity to the unresolved λ_+) is resolved, and approximates, though underestimates, the eigenvalue splitting $\Delta\lambda_{\pm}$ (i.e., $\Delta\omega_{\text{peaks}}^{(b)}/2\pi = 110$ MHz, while $\Delta\lambda_{\pm}/2\pi = 130$ MHz).

Figures 5.4 (c), d show measured spectra for both the bare-cavity with no atoms (NA), $R_{\text{NA}}(\Delta_{pa})$ and $T_{\text{NA}}(\Delta_{pa})$, and with triggered single atoms (A), $R_{\text{A}}(\Delta_{pa})$ and $T_{\text{A}}(\Delta_{pa})$, for $\Delta_{ca}/2\pi = 60$ MHz. The splitting $\Delta\omega_{\text{exp}}/2\pi \approx 95 \pm 5$ MHz between the prominent cavity peak and the dressed state feature can be read directly from both T_{A} and R_{A} . Taking $\Delta\omega_{\text{peaks}}^{(c,d)}$ as a lower estimate for the average eigenvalue splitting $\Delta\lambda_{\pm}$ yields an average coupling $\bar{g}/2\pi \gtrsim 37 \pm 3$ MHz. This average coupling indicates that strong coupling is achieved on average, with $\bar{g} > (\kappa, \gamma_0)$, where $(\kappa, \gamma_0)/2\pi = (21, 2.6)$ MHz.

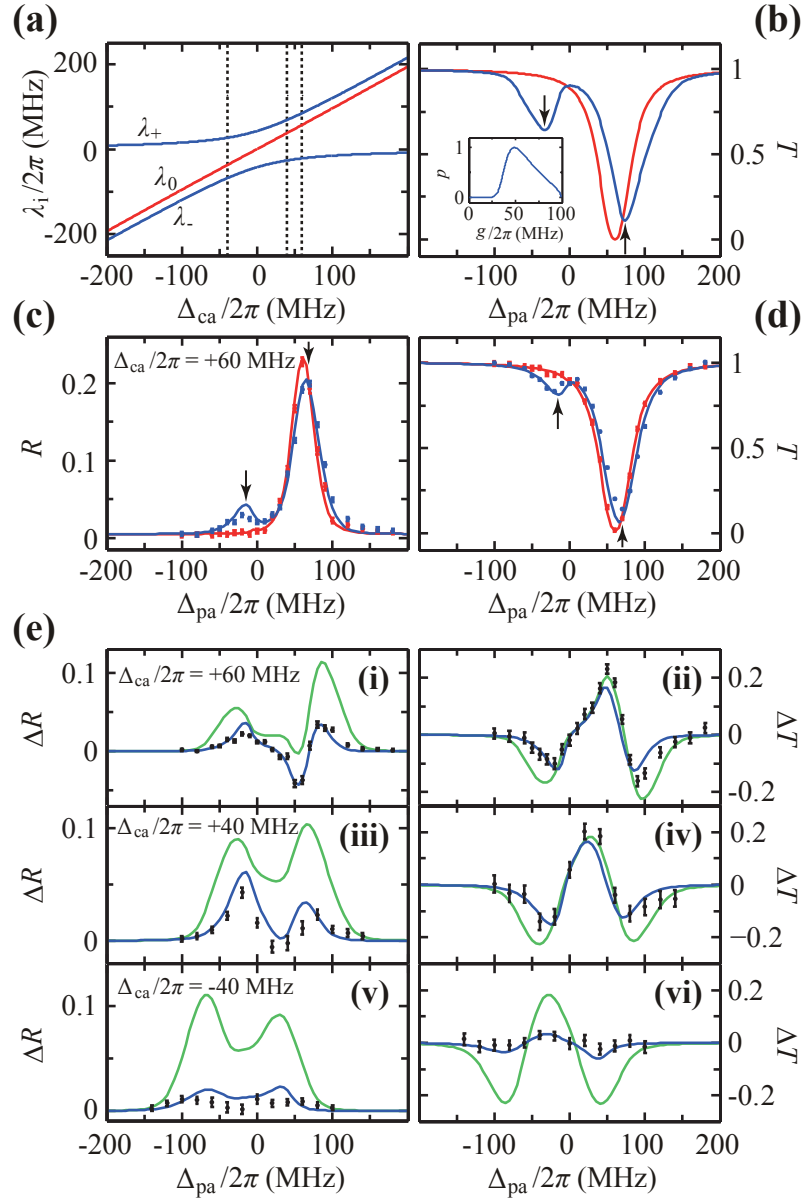


Figure 5.4: **Transmission $T(\omega_p)$ and reflection $R(\omega_p)$ spectra for single atoms coupled to a microtoroidal resonator.** (a) cQED eigenvalues $\lambda_{\pm,0}$ for $\{h, g\}/2\pi = \{10, 40\}$ MHz as a function of atom-cavity detuning Δ_{ca} . The dashed lines indicate the detunings for the spectra in the following panels. (b) $T_i(\omega_p)$ for $\Delta_{ca}/2\pi = +60$ MHz for the empty cavity $i = \text{NA}$ (red) and with atoms $i = \text{A}$ (blue) calculated from a simple average for falling atoms over the distribution $p_{\text{fall}}(g)$ (inset) absent cavity and surface forces. $\Delta\omega_{\text{peaks}}$ is computed from the frequency difference for the peaks indicated by arrows. (c-d) Experimental reflection $R_i(\Delta_{pa})$ and transmission $T_i(\Delta_{pa})$ spectra with the peaks used for $\Delta\omega_{\text{exp}}$ indicated. Curves are results of the full Monte Carlo simulation and the color scheme is the same as in panel b. e Difference spectra $\Delta R = R_{\text{A}}(\Delta_{pa}) - R_{\text{NA}}(\Delta_{pa})$ and $\Delta T = T_{\text{A}}(\Delta_{pa}) - T_{\text{NA}}(\Delta_{pa})$ for $\Delta_{ca}/2\pi = +60$ (i,ii), $+40$ (iii,iv), -40 MHz (v,vi). Green lines are simulation results for $U_s = U_d = 0$, while blue lines are from the complete simulation. Error bars are estimated from photon counting statistics and systematic uncertainties.

Quantitative differences between the simple model in Fig. 5.4 (b) and the experimental spectra in Fig. 5.4 (c-d) yield information about additional effects, including perturbative surface interactions not included in the standard Jaynes-Cummings treatment [9, 57]. In particular, the feature at $\Delta_{\text{pa}}/2\pi = -30$ MHz in both R_A and T_A is significantly reduced in magnitude from the spectrum predicted by $p_{\text{fall}}(g)$, which as discussed below, results from the effects of $\{U_s, U_d\}$ on the atomic trajectories and internal levels as in Figs. 5.2, 5.3.

Measurements of the difference spectra taken with and without atom transit events, $R_A - R_{\text{NA}}$ and $T_A - T_{\text{NA}}$ are shown in Figs. 5.4 (e) for cavity detunings $\Delta_{\text{ca}}/2\pi = 60, 40, -40$ MHz. Again, the simple prescription of reading $\Delta\omega_{\text{peaks}}$ directly from the splitting of the low and high frequency peaks together with the expression for $\Delta\lambda_{\pm}$ leads to an estimate of the average coupling $\bar{g}/2\pi \gtrsim 35 \pm 5$ MHz that is consistent across the six spectra displayed.

For comparison to the measured spectra, the full curves in Figs. 5.4 (e) are from our Monte Carlo simulation for $\Delta R \equiv R(\Delta_{\text{pa}}) - R_{g \rightarrow 0}(\Delta_{\text{pa}})$ and $\Delta T \equiv T(\Delta_{\text{pa}}) - T_{g \rightarrow 0}(\Delta_{\text{pa}})$. Calculated spectra are shown both for the full model and with all forces removed. Agreement with the full model is achieved for the choice $g_{\text{max}}/2\pi \sim 100$ MHz, which is somewhat less than the value of $g_{\text{max}}/2\pi = 140$ MHz expected for the fundamental TE mode near $\lambda = 852$ nm estimated from a finite element calculation (Fig. 5.1 (b)). The difference is attributable to imprecise knowledge of the toroid geometry and mode. Except for the relevant detunings and measured cavity decay rates, the same parameters are used for each spectrum simulation; specifically, $(g_{\text{max}}, \gamma_0)/2\pi = (100, 2.6)$ MHz. Note that apart from the adjustment of g_{max} , all parameters in the simulation are estimated from measurements or, in the case of dipole forces, surface forces, and level shifts, are taken from theoretical and experimental results in the literature (see Sec. 5.10).

For each of the spectra in Fig. 5.4 (e), removing the Casimir-Polder and dipole forces (i.e., setting U_s, U_d to zero) leads to increased deviations from the measured spectra relative to the full simulation, which describes the measurements reasonably well. The most significant effect of U_s is seen for a red-detuned cavity ($\Delta_{\text{ca}}/2\pi = -40$ MHz) where significant spectral features not readily observed in the data appear for $U_s = 0$. In combination with the temporal analysis in Figs. 5.2, 5.3, the cQED spectra in Fig. 5.4 (e) illustrate the necessity of including perturbative surface interactions for understanding atomic dynamics near the resonator. The model uses a distance dependent atomic decay rate $\gamma_{\parallel}(d)$ for our linearly polarized TE mode, but the differences between γ_{\parallel} and γ_0 are too small to be observed in the data. Despite the overall consistency achieved with the full simulation, systematic disagreements between data and model suggest that further analytical progress is required, including

better (independent) knowledge of the toroid geometry, as well as solving the full master equation to account for the multi-level structure of the Cs atom[26] (see Sec. 5.10).

5.7 Photon statistics

To confirm the quantum nature of the atom-cavity interaction near the surface of the toroid, we present in Fig. 5.5 measurements of photon statistics for the transmitted field P_T for $\Delta_{ca} = 0$. Photon statistics are inferred from the time records $C_{1,2}(t_i)$ of photoelectric counts in time bins t_i for two detectors D_1, D_2 following an atomic trigger event at $t = 0$. Fig. 5.5 shows the average cross-correlation $C_{12}(\tau) = \sum_i \langle C_1(t_i) C_2(t_i + \tau) \rangle$ for $0 < t_i < 8 \mu s$ as well as the cross-correlation of the average counts $\bar{C}_{12}(\tau) = \sum_i \langle C_1(t_i) \rangle \langle C_2(t_i + \tau) \rangle$, where the angled brackets represent sums over the ensemble of triggers. The photon process is super-Poissonian, indicated by $C_{12}(\tau) > \bar{C}_{12}(\tau)$ for all τ , due to large fluctuations in transmitted intensity from one atom to the next, which presumably arise from variations in atomic position \vec{r} and hence coupling $g(\vec{r})$ near the toroid's surface (inset (i)). Even in the face of these large fluctuations, the non-classical character of the atom-cavity interaction survives, as is evident from the short-time dynamics shown in Fig. 5.5, where $C_{12}(0) < C_{12}(\tau)$ exhibits photon antibunching. From the minimum at $\tau = 0$, $C_{12}(\tau)$ regresses to its peak with characteristic half-width of 6 ns.

In contrast to the case $C_{12} \rightarrow 0$ realized in microtoroids in the bad-cavity limit for a photon turnstile [57] and a photon router [10], here $C_{12}(0)$ is 0.55 of its maximum value, which results from coherent dressed-state dynamics for $\Delta_{ca} = 0$. Averaging a time-dependent calculation of the coincidence count rate for a fixed value of g over the distribution of g obtained from our trajectory simulations results in reasonable agreement with our measurements (red curve in Fig. 5.5), with the only free parameter being the overall amplitude which is scaled to match the data. Our model predicts both $C_{12}(0) \neq 0$ and the regression timescale near $\tau = 0$, which supports its effectiveness in describing the quantum behavior of the atom near the surface of the toroidal resonator.

5.8 Detailed microtoroid cQED theory

Here we outline a basic cQED theoretical model for an atom coupled to a cylindrically symmetric whispering gallery resonator as originally presented in the supplementary material of Refs. [9] and [57] and shown schematically in Fig. 5.6 (also see Fig. 3.1 a-b)). A microtoroidal cavity supports two degenerate counter-propagating whispering gallery modes at resonance frequency ω_c with anni-

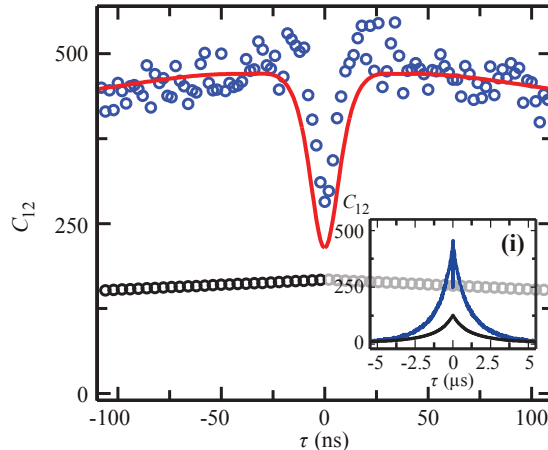


Figure 5.5: **Photon statistics for localized atoms with $\Delta_{\text{ca}} = 0, \Delta_{\text{pa}} = 0$.** Cross-correlation $C_{12}(\tau)$ (blue circles) computed from the records of photoelectric counts at detectors D_1, D_2 from the forward flux P_{T} from a sum over many atom trajectories showing photon antibunching around $\tau = 0$, with $\overline{C}_{12}(\tau)$ obtained from the product of averages of the recorded counts at each detector for comparison (black circles). The red curve is a calculation for the two-time second-order correlation function from the full simulation scaled by a single parameter to match $C_{12}(\tau)$ at $\tau = \pm 40$ ns. (i) Expanded view of $C_{12}(\tau)$ and $\overline{C}_{12}(\tau)$ over full range of τ , with the long decay time of $\sim 2 \mu\text{s}$ originating from the atom transit times (Fig. 2a) and the classical variance between transits.

hilation operators a and b , which are coupled via scattering at a rate h [223]. Each travelling-wave mode has an intrinsic loss rate, κ_i , due to absorption, scattering, and radiation. A tapered fiber carries input fields $\{a_{\text{in}}, b_{\text{in}}\}$ at frequency ω_p which couple to the cavity modes with an extrinsic coupling rate κ_{ex} . The output fields of the fiber taper can be written in terms of the input fields as $\{a_{\text{out}}, b_{\text{out}}\} = -\{a_{\text{in}}, b_{\text{in}}\} + \sqrt{2\kappa_{\text{ex}}}\{a, b\}$ [9, 57]. For single-sided excitation, $\langle b_{\text{in}} \rangle = 0$ and a_{in} drives the a mode with strength $\varepsilon_p = i\sqrt{2\kappa_{\text{ex}}}\langle a_{\text{in}} \rangle$. The transmitted and reflected photon fluxes, $P_{\text{T}} = \langle a_{\text{out}}^\dagger a_{\text{out}} \rangle$ and $P_{\text{R}} = \langle b_{\text{out}}^\dagger b_{\text{out}} \rangle$, are calculated from the input flux $P_{\text{in}} = \langle a_{\text{in}}^\dagger a_{\text{in}} \rangle$, with the transmission and reflection coefficients defined as $T = P_{\text{T}}/P_{\text{in}}$ and $R = P_{\text{R}}/P_{\text{in}}$, respectively.

We consider a two-level atom with transition frequency ω_a at location $\vec{r}(\rho, \phi, z)$ (in standard cylindrical coordinates) coupled to the travelling wave modes $\{a, b\}$ with single-photon coupling rate $g_{\text{tw}}(\vec{r}) = g_{\text{tw}}^{\text{max}} f(\rho, z) e^{\pm i\theta}$, where $f(\rho, z)$ is a function determined by the cavity mode, $\theta = k\rho\phi$, and k is the wavevector of the circulating mode. The atomic frequency ω_a may in general be shifted by frequency δ_a from the vacuum frequency due to interactions with the surface of the dielectric resonator. An approximate form for the function $f(\rho, z)$ for the lowest order toroid mode in the evanescent region can be written as $f(\rho, z) \sim e^{-d/\lambda} e^{-(z^2/w_z)^2}$ where $d = d(\rho, z)$ is the closest distance to the toroid surface, w_z is a vertical distance scale, and λ is the wavelength over 2π .

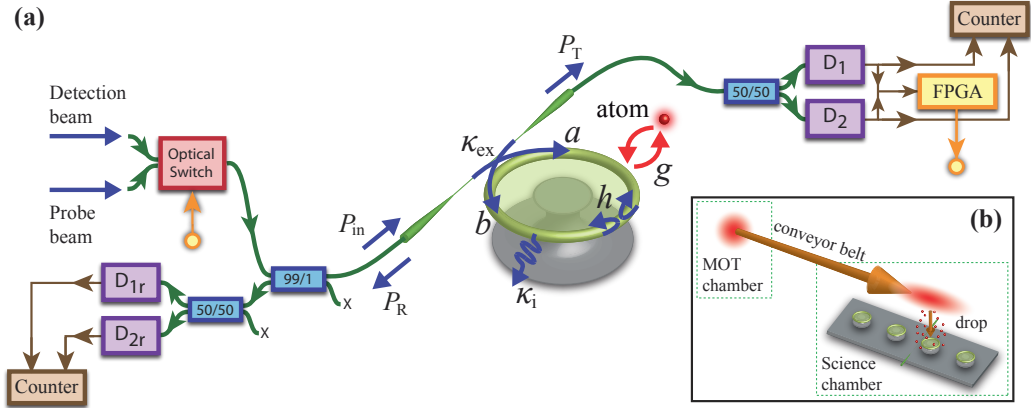


Figure 5.6: **Schematic of microtoroidal cQED system.** (a) A microtoroidal resonator supports counter-propagating travelling wave modes $\{a, b\}$ coupled at a rate h . The circulating fields decay at a rate $\kappa = \kappa_i + \kappa_{\text{ex}}$ where κ_i is the resonator intrinsic loss rate and $\kappa_{\text{ex}} = \sqrt{\kappa_i^2 + h^2}$ is the coupling rate between the cavity and a tapered fiber at critical coupling. An optical switch controlled by an FPGA selects a driving field conditioned upon detection of an atom coupled to the cavity normal modes at a rate g . The all-in-fiber switch and beam splitter network delivers a power P_{in} to the microtoroid. Transmitted power P_{T} and reflected power P_{R} are detected by four single photon counting modules (SPCMs) and digitally recorded by a counter card. (b) A cloud of cesium atoms from a separate ‘MOT chamber’ is transferred via a differential pumping tube by an optical conveyor belt into the ‘science chamber’ and released $800 \mu\text{m}$ above a microtoroid.

The Hamiltonian in a frame rotating at ω_{p} is given by [9, 57]:

$$\begin{aligned}
 H/\hbar = & \Delta_{\text{ap}}\sigma^+\sigma^- + \Delta_{\text{cp}}(a^\dagger a + b^\dagger b) + h(a^\dagger b + b^\dagger a) + (\varepsilon_{\text{p}}^* a + \varepsilon_{\text{p}} a^\dagger) \\
 & + (g_{\text{tw}}^* a^\dagger \sigma^- + g_{\text{tw}} \sigma^+ a) + (g_{\text{tw}} b^\dagger \sigma^- + g_{\text{tw}}^* \sigma^+ b), \quad (5.1)
 \end{aligned}$$

where σ^\pm are the atomic raising and lowering operators, $\Delta_{\text{ap}} = \omega_{\text{a}} - \omega_{\text{p}}$ and $\Delta_{\text{cp}} = \omega_{\text{c}} - \omega_{\text{p}}$.

Dissipation is treated using the master equation for the density operator of the system ρ :

$$\begin{aligned}
 \dot{\rho} = & -\frac{i}{\hbar}[H, \rho] + \kappa(2a\rho a^\dagger - a^\dagger a\rho - \rho a^\dagger a) + \kappa(2b\rho b^\dagger - b^\dagger b\rho - \rho b^\dagger b) \\
 & + \gamma(2\sigma^-\rho\sigma^+ - \sigma^+\sigma^-\rho - \rho\sigma^+\sigma^-). \quad (5.2)
 \end{aligned}$$

Here, $\kappa = \kappa_i + \kappa_{\text{ex}}$ is the total field decay rate of each cavity mode, and $2\gamma(\vec{r})$ is the atomic spontaneous emission rate, which is orientation dependent near a dielectric surface (Sec. 6.2.4.1). The Hamiltonian (Eq. 5.1) can be rewritten in a standing wave basis using normal modes $A = (a+b)/\sqrt{2}$

and $B = (a - b)/\sqrt{2}$,

$$\begin{aligned} H/\hbar = & \Delta_{\text{ap}}\sigma^+\sigma^- + (\Delta_{\text{cp}} + h)A^\dagger A + (\Delta_{\text{cp}} - h)B^\dagger B + (\varepsilon_{\text{p}}^*A + \varepsilon_{\text{p}}A^\dagger)/\sqrt{2} \\ & + (\varepsilon_{\text{p}}^*B + \varepsilon_{\text{p}}B^\dagger)/\sqrt{2} + g_{\text{A}}(A^\dagger\sigma^- + \sigma^+A) - ig_{\text{B}}(B^\dagger\sigma^- - \sigma^+B), \end{aligned} \quad (5.3)$$

where $g_{\text{A}}(\vec{r}) = g_{\text{max}}f(\rho, z)\cos(\theta)$, $g_{\text{B}}(\vec{r}) = g_{\text{max}}f(\rho, z)\sin(\theta)$, and $g_{\text{max}} = \sqrt{2}g_{\text{tw}}^{\text{max}}$. Depending on the azimuthal coordinate θ , coupling may occur predominantly, or even exclusively, to one of the two normal modes. For such θ , the system can be interpreted as an atom coupled to one normal mode in a traditional Jaynes-Cummings model with dressed-state splitting given by the single-photon Rabi frequency $\Omega_{(1)} = 2g \equiv 2g_{\text{max}}f(\rho, z)$, along with a second complementary cavity mode not coupled to the atom. For a fixed phase of h set by the scattering in the toroid, this decomposition is not possible for arbitrary atomic coordinate θ ; for non-zero h the atom in general couples to both normal modes.

The master equation can be numerically solved using a truncated number state basis for the cavity modes. For a sufficiently weak probe field, the Eq. (5.2) can be linearized to find equations of motion for the field amplitudes. Note that while the detunings Δ_{cp} and Δ_{ap} in these theoretical expressions are referenced to the probe frequency, those used in the sections prior to Sec. 5.8 in this chapter are referenced to the frequency of the $6S_{1/2}, F = 4 \rightarrow 6P_{3/2}, F' = 5$ transition of Cs.

5.9 Experiment scheme and setup

A silicon chip with 10-30 silica microtoroids is fabricated using standard methods [11] and mounted on a thermoelectric heat pump which stabilizes the resonance frequency ω_{c} for the mode of interest to within ~ 1 GHz of ω_{a} . The cavity resonance frequency ω_{c} is tuned using the silicon substrate temperature to be near the $6S_{1/2}, F = 4 \rightarrow 6P_{3/2}, F' = 5$ transition of Cs at frequency $\omega_{\text{a}}^{(0)}$. The microtoroid used in the experiment has a major diameter of $D_{\text{M}} \approx 24 \mu\text{m}$, minor diameter of $D_{\text{m}} \approx 3 \mu\text{m}$, and a quality factor $Q \sim 10^7$. A finite element model of the fundamental TE mode for this geometry gives a mode volume of $\sim 100 \mu\text{m}^3$, corresponding to maximum atom-cavity coupling for linear polarized light of $g_{\text{max}}/2\pi \approx 100$ MHz at the toroid surface (i.e., a maximum single-photon Rabi frequency $\Omega_{\text{max}}^{(1)}/2\pi = 2g_{\text{max}}/2\pi \approx 200$ MHz). The parameters for the $\Delta_{\text{ca}} = 0$ and $\Delta_{\text{ca}}/2\pi = 60$ MHz measurements are $(\kappa_{\text{i}}, h, \kappa_{\text{ex}})/2\pi = (8, 10, 12.8)$ MHz, and for the $\Delta_{\text{ca}}/2\pi = \pm 40$ MHz measurements are $(\kappa_{\text{i}}, h, \kappa_{\text{ex}})/2\pi = (13.5, 11, 17.4)$ MHz. For the results of Ref. [5], the typical intracavity photon number is $\bar{n} \lesssim 0.1$ in the absence of an atom and the effective mean atom-cavity

coupling is $\bar{g}/2\pi \approx 40$ MHz. For $\kappa/2\pi \sim 20$ MHz, the critical photon number $n_0 \approx \gamma_0^2/2\bar{g}^2 \sim 10^{-3}$ and critical atom number $N_0 \approx 2\gamma_0\kappa/\bar{g}^2 \sim 10^{-2}$ are both less than unity. Therefore, the system is in the single photon, strong coupling regime.

The experimental setup is similar to that in Refs. [9] and [57] and is illustrated in Fig. 5.6. Briefly, cesium atoms are magneto-optically cooled and trapped below 10 μK in an ‘MOT chamber’, then loaded into an optical conveyor belt [140], and transported over 20 cm into a ‘Science chamber’ (at $< 10^{-9}$ torr) through a differential pumping tube to limit cesium contamination on the microtoroids [10]. This cloud of $\sim 10^7$ atoms at temperature $T \approx 100$ μK is dropped 800 μm directly above a microtoroid. Access to the input and output light fields of the microtoroid is provided by a tapered optical fiber. The taper and toroid chip are mounted on piezoelectric-driven stages inside the ‘Science’ chamber which enable stable tuning of κ_{ex} to the critical coupling condition $\kappa_{\text{ex}} = \sqrt{\kappa_{\text{in}}^2 + h^2}$ where the transmitted output field a_{out} nearly vanishes for $\Delta_{\text{cp}} = 0$. A darkness of $T = P_{\text{T}}/P_{\text{in}} \approx 0.01$ at critical coupling is actively maintained using an optical heating servo with ~ 10 -Hz bandwidth to stabilize ω_c . Typical input power is at the level of $P_{\text{in}} \sim 4$ pW at frequency ω_p .

Detection and probe beams pass through fast (~ 10 ns response) in-fiber Mach-Zehnder optical switches before entering a beam splitter network which reduces the power to P_{in} (Fig. 5.6 (a)). The transmitted beam P_{T} passes through a 50/50 beam-splitter to two single-photon counting-modules (SPCMs), $\{D_1, D_2\}$, while the reflected beam P_{R} travels back through the beam splitter network to another two SPCMs, $\{D_{1r}, D_{2r}\}$. In each experimental cycle, a detection beam with $|\omega_p - \omega_c|/2\pi < 5$ MHz is used for real-time atom detection while the atom cloud is falling (see Sec. 5.9.1). The atom cloud takes ~ 50 ms to pass the toroid, during which 1 – 10 single atom events typically lasting 2-4 μs are observed. An atom coherently coupled to the cavity at rate $g(\vec{r})$ disturbs this critical coupling condition and the photodetector counts at D_1, D_2 increase. Single photoelectric events within a running time window Δt_{th} are counted and compared with a threshold number C_{th} by a field programmable gate array (FPGA) operating at 40 MHz. For the data shown in Figs. 5.3 and 5.4, the parameters $\Delta t_{\text{th}} = 750$ ns and $C_{\text{th}} = 5$ are chosen to give a false detection rate of less than 1% and an average trigger time as early as possible during the atom transits (Sec. 5.9.1). Upon a trigger event determined by a 40-MHz field-programmable gate array (FPGA), which defines $t \equiv 0$ for each event, the FPGA sends a trigger pulse to a photon counting card to time stamp and record subsequent photodetections with 2-ns time resolution. This generates photon count time series $C_i(t)$ from detector D_i with 2-ns resolution. In addition, upon a trigger event, the fiber input is switched

from the detection to the probe beam which may have different power and/or frequency detuning as discussed below. The entire sequence from MOT loading through atom dropping takes ~ 500 ms. During the ~ 450 ms when atoms are not falling, a third beam with frequency continuously scanned over a range of ~ 1 GHz around ω_a is used to measure ω_c for the optical temperature servo. The empty cavity transmission measured with this scanning beam is also used to optimize the cavity-fiber coupling, κ_{ex} .

As discussed above, at $t = 0$, the FPGA triggers high-frequency optical modulators that switch the power and frequency of the probe input to the tapered fiber. For typical experiments, the probe flux is reduced to $P_{\text{in}} \simeq 2$ pW and the probe detuning $\Delta_{\text{pa}} = \omega_p - \omega_a^{(0)}$ set to a value within the range shown in Fig. 5.4. Including both optical and electrical delays, the optical switching is complete by $t = 150$ ns. The photocount record on detector i , $C_i(t)$, in a time interval $0 < t < 8 \mu\text{s}$ following the trigger is recorded for a succession of $N \gg 1$ trigger events. For spectral measurements, the transmitted and reflected photocount records are averaged over a selected time window (typically, $200 < t < 700$ ns) and normalized by the photocounts taken with large detuning, $P_T(\Delta_{\text{pa}} \gg \kappa)$, to obtain the experimental transmission and reflection spectra, $T(\Delta_{\text{pa}})$ and $R(\Delta_{\text{pa}})$. Error bars for data are estimated assuming Poissonian counting statistics and are written as plus or minus one standard deviation. Fit results are quoted with 68% confidence intervals.

Having validated our trajectory simulation with the measurements in Figs. 5.2-5.5, we have studied loading of falling atoms into a two-color evanescent field far off-resonance trap (FORT) (Fig. 5.3 (c)) [246, 201]. A trapping potential U_t can be formed using a blue-detuned fundamental mode and a higher order red-detuned mode [246]. For our simulation, we use a red (blue)-detuned mode near 898 nm (848 nm) with powers $\sim 50 \mu\text{W}$ each to give a trap depth of ~ 1.5 mK which is switched on at $t = 0$ conditioned on a falling atom FPGA trigger. Despite the large kinetic energy of falling atoms and poor localization of the atoms relative to the trap minimum, approximately 20% of triggered atom trajectories are captured in the trap. Simulated trapping times exceed $50 \mu\text{s}$, limited not by heating from trapping light but by the radiation pressure from unbalanced traveling whispering-gallery modes. This radiation pressure leads to atom gallery orbits around the toroid [158] (Fig. 5.3 (c)). Exciting a red-detuned standing wave would provide three-dimensional trap confinement and increase the trap lifetime.

5.9.1 Real time detection of atom transits

The temporal and spectral experiments described in Ref. [5] are realized by switching the driving laser conditioned on a single atom being coupled to the cavity to measure the response. Real-time detection and triggering of atomic transits is achieved in less than a microsecond for atom transits which typically last a few microseconds so that the optical triggering and switching occurs while the atom remains coupled to the resonator. As mentioned previous section, single-atom detection is performed at critical coupling with $P_T \leq 0.01P_{in}$. When an atom is coupled to the cavity, the cQED eigenstructure splits and P_T increases. The cavity response for $\Delta_{ca} = 0$ is shown for representative values of θ in Fig. 5.7 (a)-(b), illustrating the increase in T for $g \neq 0$ and the sensitivity to θ . The spectra vary smoothly with θ , with $\theta = 0$ the mirror image about $\Delta_{pa} = 0$ of $\theta = \pi/2$. During the 50-ms interval after Cs atoms are released, P_T is monitored by SPCMs D_1 and D_2 and analyzed in real-time by the 40-MHz FPGA. The FPGA outputs a trigger pulse when it counts a threshold C_t single-photon pulses in a running time window of length Δt . The trigger gates the photon counting card as well as controls the optical switch network. Signal logic, electrical and optical travel times, and optical switch times introduce a latency of approximately 100 – 150 ns between trigger and modulation of probe beam parameters at the toroid.

Figures. 5.7 (c) and (d) show the total transmitted flux $\sum_i (C_1(t) + C_2(t))$ summed over 1501 triggers using $C_t = 4$ and $\Delta t = 750$ ns. Instead of switching the input beam upon a trigger event, the FPGA trigger times are digitally recorded along with the photon counts. In part (c), the time series $C_1(t) + C_2(t)$ for each trajectory is aligned such that the trigger occurs at $t = 0$. The sharp peak just before $t = 0$ has a width of ~ 50 ns, corresponding to the last (fourth) photon count that generated the trigger within the last 25-ns FPGA time step for every trigger. The previous three photon counts are distributed within the 750 ns window prior to the trigger. Note that 25 ns prior to this window, $C_1 + C_2 = 0$ because if there was a count here, then the transit criteria would have been satisfied one 25-ns time step earlier. These classical detection biasing effects are not indicative of cQED dynamics of the microtoroidal system. In part (d), the origin is shifted for each trigger individually so that $t = 0$ corresponds to the weighted mean of photon arrival times for $\pm 10 \mu\text{s}$ around each trigger event. The distribution of the 1501 events shows that most of the triggers occur near the peak of $C_1 + C_2$. For experiments, the trigger parameters C_t and Δt are chosen so that the false detection rate of atom triggers is below 1% and the trigger time is as early as possible relative to the peak trajectory transmission. For the experiments in Fig. 5.3 and 5.4 of Sec. 5.4 and 5.6, we use the parameters $C_t = 5$ and $\Delta t = 750$ ns.

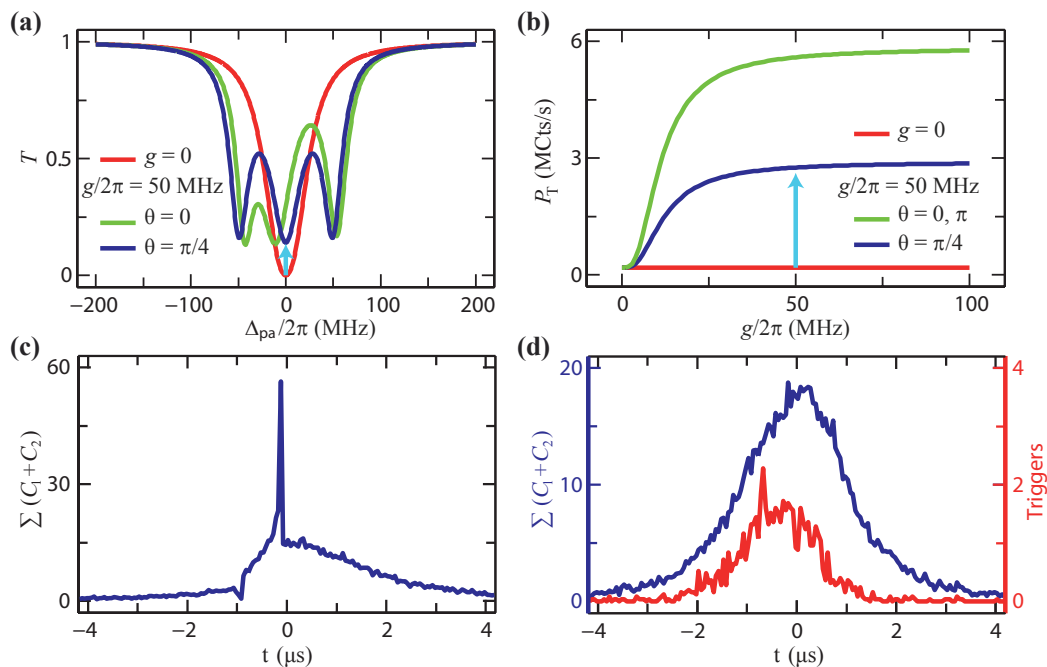


Figure 5.7: **Real time detection of single atom transits.** (a) Normalized transmission spectra $T(\Delta_{\text{pa}})$ as a function of probe detuning Δ_{pa} for $g = 0$ and $g/2\pi = 50$ MHz ($\theta = 0$ and $\theta = \pi/4$) at critical coupling. The spectrum for $\theta = \pi/2$ is the mirror image of the $\theta = 0$ case about the $\Delta_{\text{pa}} = 0$ axis. (b) Transmitted photon flux as a function of g for $\Delta_{\text{pa}} = 0$. An atom trajectory with increasing g (say from $g = 0$ to $g/2\pi = 50$ MHz) results in increased P_T illustrated by the cyan arrow. (c) Experimental counts $C_1(t) + C_2(t)$ for 1501 transits from 596 atom drops with 4% false detection rate where the triggers are aligned at $t = 0$. (d) The same data aligned by redefining $t = 0$ to be the mean photon arrival time for each individual transit (blue). This alignment removes selection biasing seen in panel (a) and allows plotting of the distribution of trigger times relative to the transit center (red). Most triggers occur just prior to the peak of transmission of atom transits. The data in (c) and (d) have been smoothed for clarity, which artificially broadens the selection biasing effects in (c). In (b), (c) and (d) the maximum off-resonant transmitted photon flux is $P_T \approx 18$ MCTs/s ~ 4 pW.

5.10 Modeling ensembles of atoms detected in real time

The stochastic nature of the detection process used in Ref. [5] introduces an ensemble of cQED parameters included in any given measurement. We present two methods in this section for understanding the resulting distributions. A simplified analytic approach gives a rough result by neglecting the details of atomic trajectories. A Monte Carlo simulation treats atomic motion in a semiclassical model to investigate the effects of atomic forces.

5.10.1 Analytic model for real time detection distributions

Here we outline a simple analytic model of the stochastic distribution $p_{\text{fall}}(g)$ of coupling parameters g observed in a real-time detection experiment. We assume atoms fall vertically through a Gaussian cavity mode so that $g(\rho, z(t)) \sim g_c(\rho)e^{-(z(t)/w_z)^2}$ with constant velocity so that $z \propto t$ where $g_c(\rho) \sim g_{\text{max}}e^{-(\rho-D_M)/\lambda}$ is the maximum coupling at closest approach. This simple approach neglects forces on the atom which significantly modify the atomic trajectories and the dynamics of real-time triggering (see Sec. 5.10.2).

Within the cQED model, the cavity transmission $T(\Delta_{\text{pa}}, g(\vec{r}))$ is a known function of probe detuning and atom location \vec{r} . For this calculation, we assume that θ is restricted to values which maximize $T(\theta)$ at cavity resonance ($\theta = \pi/2$ for $\Delta_{\text{ca}}/2\pi = +40$ MHz, for example). We also assume that the atoms are slowly moving so that the coupling at a trigger event is the only g that contributes to a spectrum. The probability density function $p_{\text{fall}}(g)$ can be estimated as the product of the probability of any atom having a particular g and the probability of a trigger event occurring for an atom with coupling g , $p_{\text{fall}}(g) \sim p_{\text{atom}}(g)p_{\text{trigger}}(g)$. An atom transit is triggered when the total detected photon counts exceeds a threshold number, C_t , within a detection time window Δt . The detection probability $p_{\text{trigger}}(g)$ is estimated from a Poisson distribution of mean count $T(g)P_{\text{in}}\Delta t$. Given the Gaussian form of $g(t)$, $p_{\text{atom}}(g)$ can be written as a product of the probability of g in an atom transit with given g_{max} and the probability of a transit to have that g_{max} , $p_{\text{max}}(g_{\text{max}})$, integrated over all g_{max} ,

$$p_{\text{atom}}(g) = \int_g^{g_{\text{max}}} p_{\text{max}}(g_c)p(g|g_c)dg_c. \quad (5.4)$$

Note that the integral has limits from g to g_{max} since g_c cannot be smaller than g . Analytic approximations for the form of $p_{\text{max}}(g_c)$ and $p(g|g_c)$ can be found from the Gaussian approximation to the mode evanescent field so that Eq. 6.17 can be evaluated (see Fig. 5.8).

5.10.2 Full Monte Carlo simulation

Analysis of experimental results which include the details of atomic trajectories is implemented with a Monte Carlo simulation of atom transits near the toroid. For each desired set of experimental parameters, a set of atomic trajectories is generated which satisfies the stochastic detection criteria. This ensemble is used to extract the cavity output functions $T(t, \Delta_{\text{pa}})$ and $R(t, \Delta_{\text{pa}})$. Parameters used in the simulation are based on direct and indirect experimental measurements and estimates as well as theoretical calculations.

Since the spontaneous emission recoil velocity $\hbar k/m \sim 0.4$ cm/s is much less than the typical velocities of falling atoms ~ 15 cm/s at $z = 0$, we use a semiclassical approximation for atomic motion. The initial atomic velocity \vec{v}_i is selected from the Maxwell-Boltzmann distribution of temperature $T = 100$ μ K and the individual trajectories are propagated forward in time. Gravity, optical dipole forces (Sec. 6.2.3), and Casimir-Polder surface interactions (Sec. 5.10.2.3) are included in the trajectory simulation. Selection logic simulating the FPGA criteria is applied to the photon counts from each trajectory, which are assumed to be Poissonian on the relevant timescales. The simulation is repeated to acquire enough triggered trajectories for a sufficient ensemble average for the final model output, which is typically at least 400 unique triggered trajectories. Spectral and temporal behaviors are calculated from the set of triggered trajectories generated for each detection criteria. The simulated output fluxes $P_T(t)$ and $P_R(t)$ are summed over the entire set of trajectories in the same time windows used for the experimental data to obtain the simulation results quoted in the text. A comparison of the distribution of g between the analytic model and the Monte Carlo simulation with and without forces appears in Fig. 5.8.

5.10.2.1 Dipole force

The dipole force is calculated from the commutator $\vec{F} = \frac{d\vec{p}}{dt} = \frac{i}{\hbar} [H, \vec{p}]$ using the Hamiltonian Eq. 5.1. In order to make this operator expression tractable, operator products are calculated as products of linearized steady-state expectation values which is approximate for weak driving power P_{in} [66, 80]. Momentum diffusion is implemented using a generalized expression for the atom-cavity diffusion tensor [170], again simplifying with linearized steady-state field expectation values. Although included in the trajectory model, diffusion is not a significant factor in falling atom trajectories at the power levels and atomic velocities in this experiment. For Fig. 5.1 of Sec. 5.2, the effective potential U_d is calculated by integrating the dipole force along the path $\rho' = \infty \rightarrow \rho$, assuming all steady-state fields change adiabatically with atom location \vec{r} .

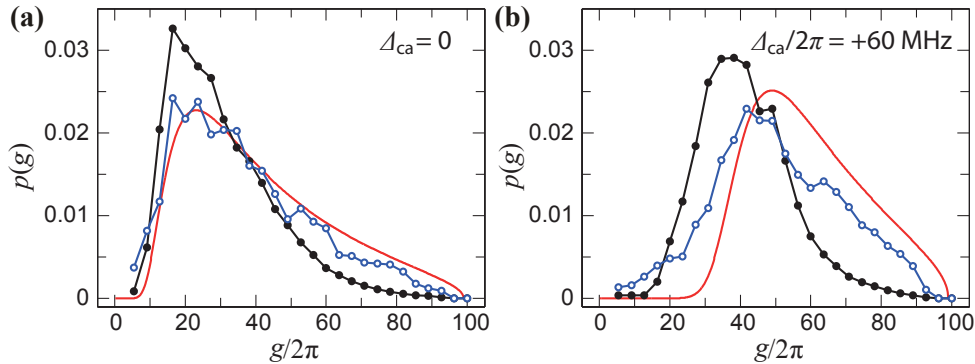


Figure 5.8: **Sample distributions $p(g)$ calculated for (a) $\Delta_{ca}/2\pi = 0$ and (b) $\Delta_{ca}/2\pi = +60$ MHz.** The analytic model is shown in red while the equivalent distribution from the Monte Carlo model with $U_d = U_s = 0$ is shown in blue. The distribution from the full Monte Carlo simulation with all potentials is shown in black for comparison. In both cases, the additional forces pull the distribution toward lower g .

5.10.2.2 Spontaneous emission rate near a surface

When a classical oscillating dipole is placed near a dielectric or metallic surface, its spontaneous emission rate is modified by the boundary. This behavior is in general oscillatory with distance d and dependent on the orientation, whether the dipole is parallel or perpendicular to the surface. The spontaneous emission rate features a marked increase within a wavelength of the surface due to available evanescent modes for decay. Calculations of $\gamma_{\parallel}(d)$ and $\gamma_{\perp}(d)$ for a planar surface used in our simulations and seen in Fig. 5.1 (b) of Sec. 5.2 follow those of Ref. [156].

5.10.2.3 Casimir-Polder interactions

Casimir-Polder (CP) interactions are important components of atomic motion for neutral atoms within a few hundred nm of a dielectric surface. For an atom located a short distance d from the dielectric, the surface potentials take the Lennard-Jones (LJ) form $U_s^{\text{LJ}} = -C_3/d^3$ where C_3 is a constant that depends on the atomic polarizability and dielectric permittivity of the surface [154, 146]. At larger distances, relativistic retardation [38] leads to a reduced potential $U_s^{\text{ret}} = -C_4/d^4$. Microtoroid cQED distance scales are set by the evanescent field scale length, $\lambda = 136$ nm for the $D2$ line of Cs. The relevant distances ($0 < d \lesssim 300$ nm) span both the LJ and retarded regimes, and consequently, the limiting power laws do not fully describe experimentally accessible CP interactions. Our model utilizes a full calculation of U_s with a Lifshitz equation approach [150, 72] valid over the entire range of d .

The CP potentials enter into our simulation in two distinct ways. First, the transition frequency

ω_a of the two-level atomic system shifts away from the vacuum frequency by $\delta_a = (U_s^{\text{ex}} - U_s^{\text{g}})/\hbar$, where U_s^{g} and U_s^{ex} are the surface potentials for the ground and excited states, respectively. Second, a force $\vec{F}_s = -\nabla U_s$ on the atom can be derived from these potentials.

We now briefly describe our calculation to find U_s^{g} for a cesium atom near a SiO_2 glass surface. The frequency dependent polarizability of the Cs ground state $\alpha(\omega)$ and the complex dielectric function $\epsilon(\omega)$ of the silica surface are needed in the Lifshitz equation. $\epsilon(\omega)$ for SiO_2 is obtained from a fit of experimental data for the complex index of refraction [185] to a seven-oscillator Lorentz model. $\alpha(\omega)$ is calculated as a sum of Lorentz oscillators over valence $6\text{S} \rightarrow \text{NP}$ transitions, with $N = 6 - 11$, whose oscillator strengths are tabulated in many sources [174]. A single high-frequency oscillator representing the Cs core polarizability is introduced with parameters such that the calculation matches the experimentally known ground state static polarizability $\alpha(0) = 5.942 \times 10^{-23} \text{ cm}^3$ [6] as well as the known ground state C_3 constant for a Cs atom near a metallic surface $C_3 = -\frac{\hbar}{4\pi d^3} \int_0^\infty \alpha(i\xi) d\xi = 4.4 \cdot \hbar \text{ kHz } \mu\text{m}^3$ [59, 117]. For U_s^{ex} we use the same core polarizability but use $6\text{P} \rightarrow \text{NS}, \text{ND}$ valence states. Curvature of the silica surface is treated following the modified method of [29] with the toroid taken as a cylinder with radius of curvature $R = D_m/2$ using the calculated material properties $\epsilon(\omega)$ and $\alpha(\omega)$. Numerical evaluation of the excited state potential U_s^{ex} is calculated in a similar manner as U_s^{g} , with an additional contribution accounting for real allowed photon exchange with the surface [79].

Figure 6.3 shows the atom-surface potential U_s^{g} for the ground state of cesium near a SiO_2 surface. For the limiting cases, our calculation yields $C_3/\hbar = 1178 \text{ Hz } \mu\text{m}^3$ and $C_4/\hbar = 158 \text{ Hz } \mu\text{m}^4$ for a planar dielectric surface. Note that the transition region between LJ and retarded regimes dominates the relevant distance scales, with U_s never fully reaching the CP power law behavior before the thermal limit takes over. For $d > D_m$, the curvature correction is no longer accurate [29], but in this regime, CP forces are already negligible to atomic motion. The excited state potential U_s^{ex} has a similar form but is larger in magnitude.

5.11 Additional cQED spectra

Figure 5.4 of Sec. 5.6 presents experimental difference spectra for various cavity detunings Δ_{ca} . For clarity, only the full simulation and a simulation with no forces are shown. Figure 5.10 displays the experimental spectra as well as additional simulations where the dipole force and CP forces are removed individually from the model. This additional figure illustrates the relative importance of force components for each experimental condition as well as the need to include both forces to achieve

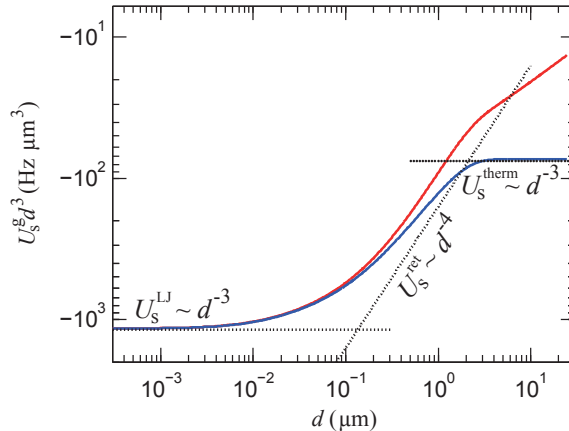


Figure 5.9: **Calculated atom-surface potential U_s^g for a Cesium atom at distance d from a SiO_2 surface with radius of curvature $R = D_m/2 = 1.5 \mu\text{m}$ (red) and $R \rightarrow \infty$ (blue).** The limiting cases for $R \rightarrow \infty$ are shown as dotted lines. In the region where surface forces are important, the cylindrical correction provides an accurate expression for the CP potentials. For $d > R$, the cylindrical correction formula is no longer valid.

agreement between simulation and data.

5.12 Summary

By exploiting real-time triggering of single atoms, our experiment has realized a system where an atom's dynamics are governed by both its strong, single-photon interactions with the resonator's field and perturbative forces on classical atomic motion, and internal level structure from proximity to the resonator's surface. Entering this regime opens the door for quantitative study of dynamical Casimir-Polder forces in the strong-coupling limit [34], which will require trapping atoms at short distance scales for extended interrogation times, for which a fiber evanescent trap is a primary candidate [17, 248]. In contrast to the standing-wave structure of a Fabry-Perot cavity [258], microtoroidal resonators offer the tantalizing possibility of radially confining an atom in a circular orbit around the toroid [158, 246], with initial results from our simulation shown in Fig. 5.3 (c). In correspondence with the development of cQED to reach the regime of strong coupling with one trapped atom in a Fabry-Perot resonator [258], the advances described here offer an important step toward trapping and cooling of a single atom near the surfaces of micro- and nano-scopic optical resonators, thereby creating an avenue for scalable on-chip quantum information science.

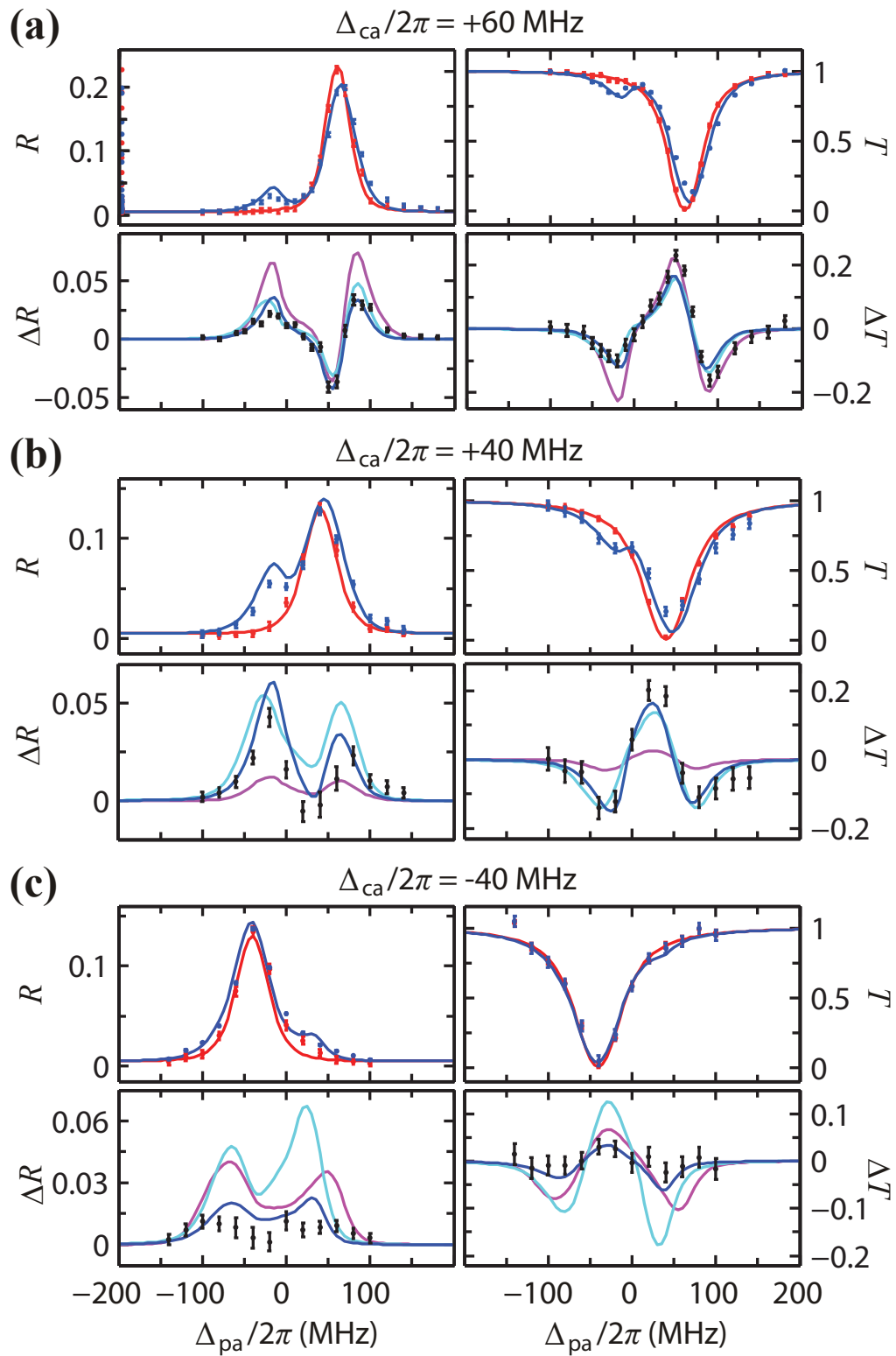


Figure 5.10: **Experimental spectral data for various cavity detuning cases:** (a) $\Delta_{ca}/2\pi = +40$ MHz. (b) $\Delta_{ca}/2\pi = -40$ MHz. (c) $\Delta_{ca}/2\pi = +60$ MHz. In each difference spectrum, we plot the simulation for the full model (blue), $U_d = 0$ (cyan), and $U_s = 0$ (magenta), and $U_d = U_s = 0$ (green). The full simulation and $U_d = U_s = 0$ cases also appear in Fig.5.4.